A&A, 701, A13 (2025)
https://doi.org/10.1051/0004-6361/202555301
© The Authors 2025

Astronomy & Astrophysics

Comparing observations of closely located JUICE and STEREO-A spacecraft during the widespread 13 May 2024 solar energetic particle event

L. Rodríguez-García[1,2,⋆], E. Palmerio[3], M. Pinto[4], N. Dresing[5], C. M. S. Cohen[6], R. Gómez-Herrero[2], J. Gieseler[5], F. Santos[4], F. Espinosa Lara[2], I. Cernuda[2], M. Mewes[1,7], C. Vallat[1], O. Witasse[8], and N. Altobelli[1]

[1] European Space Agency (ESA), European Space Astronomy Centre (ESAC), Camino Bajo del Castillo s/n, 28692 Villanueva de la Cañada, Madrid, Spain
[2] Universidad de Alcalá, Space Research Group (SRG-UAH), Plaza de San Diego s/n, 28801 Alcalá de Henares, Madrid, Spain
[3] Predictive Science Inc., San Diego, CA 92121, USA
[4] Laboratory for Instrumentation and Experimental Particle Physics (LIP), 1649-003 Lisboa, Portugal
[5] Department of Physics and Astronomy, University of Turku, FI-20014 Turku, Finland
[6] California Institute of Technology, Pasadena, CA 91125, USA
[7] Institut für Experimentelle und Angewandte Physik, University of Kiel, 24118 Kiel, Germany
[8] European Space Research and Technology Centre, European Space Agency, 2201 AZ Noordwijk, The Netherlands

Received 25 April 2025 / Accepted 30 June 2025

ABSTRACT

Context. Following its launch in April 2023, JUICE is now in its cruise phase to Jupiter, where it is scheduled to arrive in July 2031. JUICE carries a radiation monitor, namely the RADiation hard Electron Monitor (RADEM) to measure protons, electrons, and ions, detecting particles coming mainly from the anti-Sunwards direction. On 13 May 2024, a large solar energetic particle (SEP) event took place in association with an eruption close to the western limb of the Sun, as seen from Earth. Providentially, at that time, JUICE was located very close to STEREO-A, separated by only 0.13 au in radial distance, 0.3° in latitude, and 1.6° in longitude.
Aims. Our main aims are to characterise the observations within the interplanetary (IP) context whereby SEPs propagated to near-Earth, JUICE, and STEREO-A observers, while performing a first comparison of energetic particle instruments on board JUICE and STEREO-A spacecraft.
Methods. We analysed the IP context using in situ measurements and studied the proton anisotropies measured by near-Earth spacecraft and STEREO-A. We focussed on an isotropic period during the decay phase of the SEP event to compute the proton energy spectrum. We fit the STEREO-A spectrum and compared it to the one measured by SOHO and JUICE.
Results. We find the proton spectral indices measured by JUICE, SOHO, and STEREO-A to be similar. The proton fluxes measured by RADEM are in agreement with those from STEREO-A, with a deviation of less than 25%.
Conclusions. The RADEM instrument aboard JUICE is a valuable tool for measuring SEP events in the heliosphere, providing an excellent opportunity to study and characterise the energetic particle environment in the solar wind between 0.65 and 5.2 au. The intercalibration factors between the fluxes measured by STEREO-A and JUICE at the effective energies of 6.9 MeV, 13.3 MeV, 21.6 MeV, and 31.2 MeV are 1.02, 1.23, 1.12, and 0.95, respectively. We note that these intercalibration factors are valid only until 2024 July 10, when the configuration of the RADEM instrument was changed.

Key words. Sun: coronal mass ejections (CMEs) – Sun: flares – Sun: heliosphere – Sun: particle emission

1. Introduction

The Sun and its sphere of influence, the heliosphere, are characterised by a variable particle environment shaped by the dynamic solar activity. Of particular interest are so-called solar energetic particle (SEP) events, which are periods when a certain region of the heliosphere is affected by enhanced fluxes of energetic protons, electrons, and heavy ions, with the potential of damaging spacecraft electronics and delivering increased radiation to astronauts in orbit (e.g. Jiggens et al. 2014). SEPs are mainly accelerated in association with solar eruptions, such as flares and coronal mass ejections (CMEs), and are spread outwards from the Sun via a number of mechanisms that may involve particle transport along or perpendicular to magnetic field lines (e.g. Dresing et al. 2014). To enhance the physical understanding and predictive capabilities of SEPs (the current status of SEP modelling has been recently reviewed by Whitman et al. 2023), the heliophysics research community has concentrated its efforts on studying events detected by multiple spacecraft positioned at widely separated locations in the heliosphere, which can offer additional insights on particle acceleration and transport on a 'global' level (e.g. Kollhoff et al. 2021; Rodríguez-García et al. 2021; Lario et al. 2022). Given the enormous spatial scales involved and the exiguous number of probes covering different regions of the solar system, many analyses of SEP measurements in the heliosphere have been possible thanks to data from planetary missions, subsequently employed either in statistical studies (e.g. Rodríguez-García et al. 2023; Sánchez-Cano et al. 2023) or

⋆ Corresponding author: laura.rodriguezgarcia@esa.int

Open Access article, published by EDP Sciences, under the terms of the Creative Commons Attribution License (https://creativecommons.org/licenses/by/4.0), which permits unrestricted use, distribution, and reproduction in any medium, provided the original work is properly cited.
This article is published in open access under the Subscribe to Open model. Subscribe to A&A to support open access publication.

to take advantage of multi-spacecraft observations of a single event (e.g. Palmerio et al. 2021; Dresing et al. 2023; Khoo et al. 2024; Dresing et al. 2025).

The JUpiter ICy moons Explorer (JUICE; Grasset et al. 2013) spacecraft was launched on 14 April 2023 towards the largest planet in the solar system. Its goal is to perform detailed studies of its environment and that of its three ocean-bearing moons: Europa, Ganymede, and Callisto. It is equipped with remote-sensing, geophysical, and in situ instruments, and is currently on its way towards the Jovian system with expected orbit insertion in July 2031. Amongst its suite of instrumentation, JUICE carries the RADiation hard Electron Monitor (RADEM; Pinto et al. 2020; Hajdas et al. 2025), which has the capacity to measure protons, electrons, and heavier ions for the characterisation of the high-radiation Jovian particle environment. Apart from its planned planetary investigations, RADEM is operational over the whole mission's eight-year cruise phase, thereby providing an excellent opportunity to study and characterise the energetic particle environment in the solar wind between 0.65 and 5.2 au.

On 13 May 2024, a large SEP event took place in association with an eruption close to the western limb of the Sun as seen from Earth. Providentially, at that time, JUICE was close to radial alignment with the Solar Terrestrial Relations Observatory Ahead (STEREO-A; Kaiser et al. 2008) spacecraft, the heliocentric distance separating the two probes being only ∼0.13 au. Hence, this event is optimal not only to enable an analysis of a substantial particle event detected by multiple spacecraft in the inner heliosphere, but also to take advantage of SEP measurements from nearby locations for characterisation and cross-calibration purposes (e.g. Khoo et al. 2024). In this study, we present observations and analysis of the 13 May 2024 SEP event with a particular focus on measurements from JUICE, STEREO-A, and near-Earth assets, such as the Solar and Heliospheric Observatory (SOHO; Domingo et al. 1995) and the Wind (Ogilvie & Desch 1997) spacecraft. Our main aims are to characterise JUICE observations within the interplanetary (IP) context through which SEPs have propagated and to perform a cross-calibration of the energetic particle instruments on board JUICE and STEREO-A spacecraft.

In Sect. 2, we present the spacecraft positions in the heliosphere at the time of the particle event on 13 May 2024 and list the main instrumentation used in this study. Section 4 presents an overview of the solar eruption related to the particle event, which is discussed in detail in Sect. 5. In Sect. 6, we summarise and discuss our main findings. In Sect. 7, we outline our conclusions.

2. Spacecraft positions and instrumentation

An overview of the locations where different inner heliospheric probes were situated at the onset time of the 13 May 2024 event is provided in Fig. 1(a). STEREO-A (1, red) was located at 0.96 au from the Sun and ∼13° west of Earth (2, green). JUICE (6, pink) was close to radial alignment with STEREO-A at a distance of 1.09 au. Parker Solar Probe (PSP, 4, purple; Fox et al. 2016) was near its aphelion, at about 0.74 au from the Sun and ∼94° west of Earth. Solar Orbiter (5, blue; Müller et al. 2020) was located at 0.72 au and about ∼169° west of Earth. BepiColombo (3, gold; Benkhoff et al. 2021) was positioned at 0.35 au between the locations of PSP and Solar Orbiter; however, none of its instruments were collecting data during the SEP event investigated here. In particular, the spatial separation between JUICE and STEREO-A (0.13 au in radial distance, 0.3° in latitude, and 1.6° in longitude) is appropriate for a characterisation of the particle instrument on board JUICE in comparison to STEREO-A measurements.

In Fig. 1a, we see that each observer is connected to the Sun via nominal Parker field lines that employ measured solar wind speeds when available. The black arrow marks the longitude of the associated flare (W81 in Stonyhurst coordinates) and the dashed black spiral depicts the nominal magnetic field line connecting to this location. For Earth, a speed of 690 km s^{-1} has been employed based on data from the Solar Wind Experiment (SWE; Ogilvie et al. 1995) on board the Wind spacecraft, orbiting the Sun-Earth L1 point. The field line connecting STEREO-A to the Sun assumes a solar wind speed of 700 km s^{-1} according to measurements from the Plasma and Suprathermal Ion Composition (PLASTIC; Galvin et al. 2008) investigation. The same value has been employed for JUICE due to its proximity to STEREO-A. For PSP, the employed solar wind speed is 530 km s^{-1} following data from the Solar Probe Cup (SPC; Case et al. 2020), which is part of the Solar Wind Electrons Alphas and Protons (SWEAP; Kasper et al. 2016) instrument. At Solar Orbiter, the assumed ambient wind speed of 350 km s^{-1} is based on measurements from the Proton-Alpha Sensor (PAS) of the Solar Wind Analyser (SWA; Owen et al. 2020) suite. For BepiColombo, an average value of 400 km s^{-1} was used due to the lack of available plasma measurements. Finally, the field line emanating from the flare location employs a wind speed of 600 km s^{-1}, an approximately intermediate value between the speeds measured by STEREO-A and PSP. According to the heliospheric context depicted in Fig. 1a, it is clear that the locations that are best-connected to the solar eruption are STEREO-A and JUICE (footpoint separation of ∼30°), followed by Earth (footpoint separation of ∼45° to east of the flare) and PSP (footpoint separation of ∼50° to west of the flare), and, ultimately, by BepiColombo and Solar Orbiter, with the latter displaying a footpoint separation of ∼140°.

Figure 1(b) shows the corresponding ∼22 MeV proton intensities observed by different spacecraft. It employs data from JUICE/RADEM (detailed in Sect. 3) as well as those from the Energetic and Relativistic Nuclei and Electron (ERNE; Torsti et al. 1995) instrument on board SOHO, orbiting the Sun-Earth L1 point, the High Energy Telescope (HET; von Rosenvinge et al. 2008) part of the In situ Measurements of Particles And CME Transients (IMPACT; Luhmann et al. 2008) suite on board STEREO-A, the Energetic Particle Instrument-High (EPI-Hi; Wiedenbeck et al. 2017) part of the Integrated Science Investigation of the Sun (IS⊙IS; McComas et al. 2016) on board PSP, and the High-Energy Telescope (HET) part of the Energetic Particle Detector (EPD; Rodríguez-Pacheco et al. 2020) on board Solar Orbiter. The plot shows how the event features, such as flux–time profiles, onset times, and peak intensities vary across the different observers. STEREO-A and JUICE observed rapidly increasing fluxes, in agreement with their good connectivity to the eruption. Earth and PSP observed a more gradual increase in the proton flux probably due to their larger footpoint separation to the eruption location. Solar Orbiter detected a slow and modest rise in proton fluxes, consistent with its relatively poor magnetic connection to the flare's origin. This analysis concentrates on observations near 1 AU; specifically, from JUICE, near-Earth spacecraft such as Wind and SOHO, and STEREO-A, as these three locations had better magnetic connectivity to the solar event's source region. Hence, PSP and Solar Orbiter data are not included in the detailed analysis presented in this study.

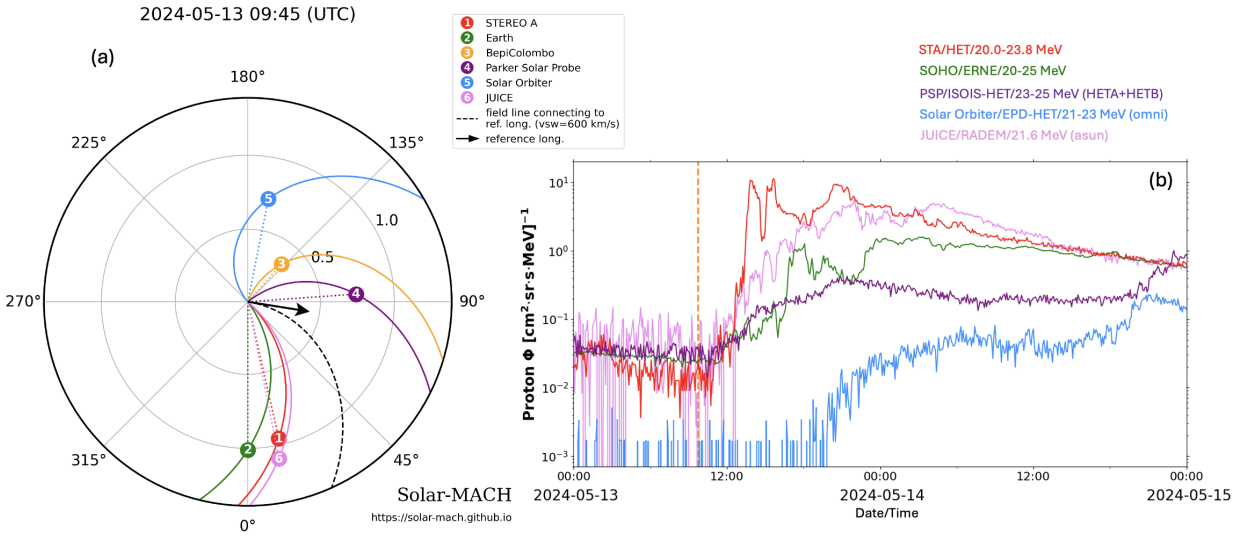

Fig. 1. Spatial distribution of spacecraft and their magnetic connectivity at 09:45 UT on 13 May 2024, along with SEP observations from multiple spacecraft. (a) The spacecraft constellation was produced using the Solar-MACH tool (Gieseler et al. 2023), which is accessible online https://doi.org/10.5281/zenodo.7016783. The solar wind speeds applied at various positions are derived from a combination of in situ measurements and estimated values, as detailed in the main text. (b) Proton intensities near 22 MeV recorded by the different spacecraft are shown. The orange vertical line marks the time of the flare's soft X-ray peak (around 09:44 UT), which is associated with the observed SEP event.

Additional observations of magnetic field, plasma, and particles were used in this study to provide context to the aforementioned data set, given by the Magnetic Field Investigation (MFI; Lepping et al. 1995), SWE, and the Three-Dimensional Plasma and Energetic Particle Investigation (3DP; Lin et al. 1995) on board Wind; Electron, Proton, and Alpha Monitor (EPAM; Gold et al. 1998) on board the Advanced Composition Explorer (ACE; Stone et al. 1998); Electron Proton Helium Instrument (EPHIN) part of the Comprehensive Suprathermal and Energetic Particle Analyser (COSTEP; Müller-Mellin et al. 1995) on board SOHO; and Magnetic Field Experiment (MFE; Acuña et al. 2008), PLASTIC, Solar Wind Electron Analyzer (SWEA; Sauvaud et al. 2008), and Low Energy Telescope (LET; Mewaldt et al. 2008) on board STEREO-A. The Particle Environment Package (PEP) and magnetometer (MAG) onboard JUICE remain inactive during the cruise phase (except for scheduled check-out windows and Earth gravity assist manoeuvres) until six months prior to Jupiter orbit insertion.

3. The RADEM instrument on board JUICE

The RADEM instrument on board JUICE has been measuring high-energy electrons and protons since September 2023. It is composed of four detectors heads: Proton Detector Head (PDH), Electron Detector Head (EDH), Heavy Ion Detector Head (HIDH), and Directional Detector Head (DDH) (Pinto 2019). Due to the configuration of its front-end electronics, at the time of the SEP event on 13 May 2024, the EDH and DDH measured both electrons and protons, while the HIDH measured both protons and other (heavy) ions. The PDH was able to measure protons with low contamination from electrons. Therefore, in this analysis, we chose to focus only on PDH measurements. We note that all channel configurations were changed in July 2024 to improve particle and energy discrimination. Therefore, the analysis discussed here only applies to SEP events before that date and with the conditions explained below.

The PDH instrument is an eight-sensor silicon stack detector pointing anti-sunward, away from the JUICE–Sun line of sight, with a 20° field of view. We note that the RADEM instrument is oriented away from the Sun, due to the spacecraft thermal constraints during the cruise phase and its location in the +X panel of the spacecraft. At the time of the SEP event onset, the PDH was working in single coincidence mode, meaning that each detector worked independently. This means that all eight sensors (channels) measured protons with energies above a threshold energy, as described in (Pinto 2019). Moreover, protons above 70 MeV are capable of penetrating the walls of the PDH collimator and reach the sensors. Therefore, each PDH channel alone was not capable of discriminating proton energies, working essentially as an integral energy channel. However, by linearly combining channels, as summarised in Col. 1 of Table 1 and applying a bow-tie method (e.g. Raukunen et al. 2020), as summarised below, we were able to generate four differential energy proton channels. These channels were chosen based on their respective signal-to-background ratio. Since the second proton detector threshold was set very low, it had a large background, most likely due to electronic noise. To decrease the effect of background counts, we subtracted the average count rate of each channel from a quiet period, namely the day of 6 May 2024.

Since the response to protons above 70 MeV is different for each proton bin, we applied the bow-tie method using the channel response functions up to this energy only (70 MeV). The response functions were derived using the GEometry ANd Tracking (GEANT4) simulation toolkit (Allison et al. 2016), with simulation parameters as detailed in Pinto (2019). The observed counting rate of a detector can be approximated as $R = j(\mathrm{Eff}) \cdot G \cdot dE$, where Eff is the effective energy, G is the channel geometric factor, and dE is the channel width. If we assume the flux spectrum to be a power law of energy, the bow-tie analysis method can find a unique solution for the Eff and $G \cdot dE$, independent of the spectral index of the SEP event. The spectral indices $[-5,-2]$ encompass the majority of SEP events. As described by Raukunen et al. (2020), we adjusted the power-law index in 0.1 steps within the specified range and derived a set of effective-energy-dependent $G \cdot dE$ curves that converged centrally, creating a characteristic 'bow-tie' pattern (Van Allen et al.

Table 1. List of linearly combined RADEM/PDH channels with their respective proton energy ranges and effective energy.

Channel Combination	Energy Range (MeV)	Effective Energy (MeV)	GdE (cm^2 sr MeV)	δ_G^- (%)	δ_G^+ (%)
(1)	(2)	(3)	(4)	(5)	(6)
1x[Proton_Bin_1] – 1x[Proton_Bin_3]	5.35–14.4	6.9	0.214	−1.22	3.00
1x[Proton_Bin_2] – 1x[Proton_Bin_4]	8.75–22.8	13.3	0.837	−9.31	24.6
1x[Proton_Bin_3] – 1x[Proton_Bin_5]	14.5–37.4	21.6	1.22	−6.53	17.93
1x[Proton_Bin_4] – 1x[Proton_Bin_5]	22.8–36.6	31.2	0.844	−2.91	8.58

Notes. Col. 1: Linear combination of proton channels used to create differential channels. Col. 2: Energy range of the proton channel. Col. 3: Effective energy obtained with the bow-tie method. Col. 4: Mean value of the geometric factor distribution calculated with the bow-tie method. Cols. 5 and 6: 5th and 95th percentile of the geometric factor distribution subtracted from the mean value in percentage calculated with the bow-tie method. Details are given in the main text.

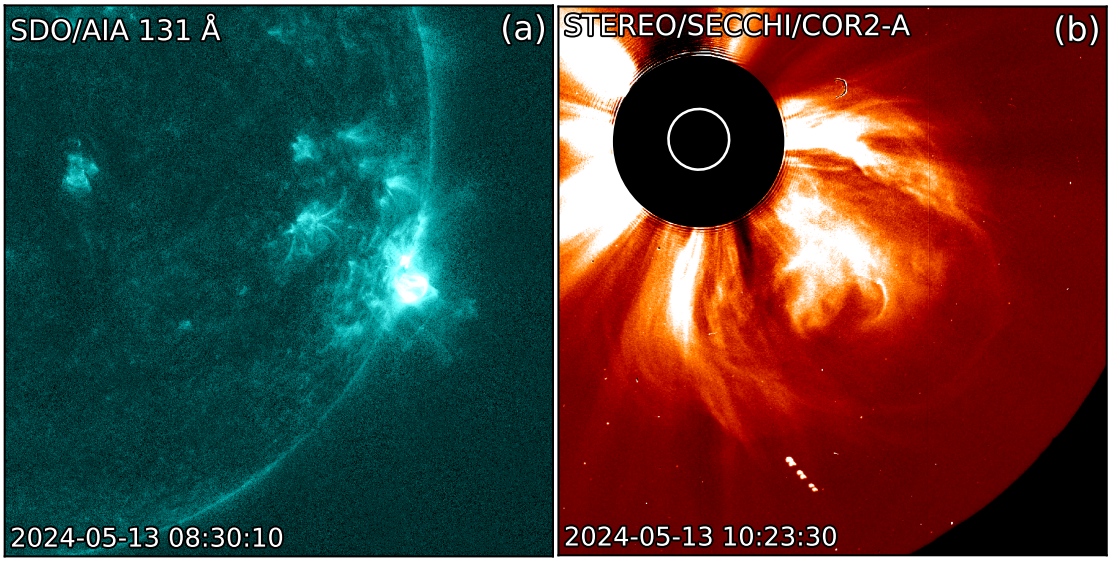

Fig. 2. Overview of several of the available remote-sensing observations for the 13 May 2024 eruption. (a) SDO/AIA image in the 131 Å channel showing AR 13664 and the eruption onset in the southwestern quadrant of the solar disc. (b) Coronagraph image from the COR2 telescope onboard STEREO-A displaying the CME as it propagated through the solar corona.

1974). The point of convergence represents the optimal values for both the effective energy (Eff) and $G \cdot dE$ within the range of power-law spectra considered. This optimal point is identified by minimising the spread between the 95th percentile (δ_G^+) and the 5th percentile (δ_G^-) of the $G \cdot dE$ values.

We note that this reconstruction is only valid for SEPs with negligible proton fluxes above 70 MeV and for observations made between September 2023 and 10 July 2024, as discussed above. Additionally, while this method finds a unique value of $G \cdot dE$ to reconstruct the flux independently of the spectral index, the response of each channel still depends on it. Therefore, the quality of the reconstruction is influenced by the spectral shape at each moment in time. Table 1 shows the results using the bow-tie method, showing the four resulting channels (Col. 1), the energy ranges (Col. 2), the effective energies (Eff, Col. 3), and the mean geometric factor ($G \cdot dE$, Col. 4), as well as the 5th (δ_G^-, Col. 5), and 95th (δ_G^+, Col. 6) percentiles of the geometric factor. The quality of the data reconstruction is better for the lowest (6.9 MeV) and highest (31.2 MeV) energy channels, which have the lowest geometric factor dispersion in relation to the spectral index, as can be seen in Cols. 5 and 6 of Table 1.

4. Overview of the solar eruption

As described in detail by, for example, Liu et al. (2024) and Weiler et al. (2025), the Sun exhibited considerable activity in May 2024. A large and complex National Oceanic and Atmospheric Administration (NOAA) active region (AR) 13664 appeared from the eastern limb as seen from Earth on 30 April and disappeared behind the western limb on 13 May. As it rotated with the Sun, AR 13364 produced a series of M- and X-class solar flares and CMEs. The SEP event under analysis is related to an M6.6 flare and associated CME erupting on the western limb at the beginning of day 13 May. We summarise here the relevant information concerning this eruption, along with an overview of some available remote-sensing observations is provided in Fig. 2.

4.1. The flare

The source region, AR 13664, located at S17W81 in Stonyhurst coordinates, and the onset of the 13 May 2024 eruption as observed from Earth orbit by the Atmospheric Imaging Assembly (AIA; Lemen et al. 2012) on board the Solar Dynamics Observatory (SDO; Pesnell et al. 2012) in the 131 Å channel are shown in Fig. 2a. The associated M6.6-class flare was of long duration, with start time at 08:48 UT, peak time at 09:44 UT, and end time at 10:57 UT. The GOES X-Ray flux in the top panel of Fig. 1 in Kruparova et al. (2024) shows the flux increase related to the flare under study (approximately mid day of 13 May). The second and third top panels of Fig. 1 in Kruparova et al. (2024) show the Type III radio bursts as observed by Wind/WAVES and

STEREO-A/WAVES, indicating that electrons escaped from the flare eruption outwards through IP space.

4.2. The coronal mass ejection

Figure 2b shows an image from the COR2 coronagraph part of the Sun Earth Connection Coronal and Heliospheric Investigation (SECCHI; Howard et al. 2008) suite on board STEREO-A. It displays the CME associated with the flare eruption as it propagated through the solar corona. The CME parameters were estimated by Liu et al. (2024) using the graduated cylindrical shell (GCS; Thernisien et al. 2006, 2009) technique, which assumes a croissant-like morphology for CMEs with two ends anchored at the Sun. The GCS model utilises observations from multiple vantage points (specifically, from STEREO-A and SOHO in this case) to reduce projection-related distortions when characterising the CME, particularly with respect to its de-projected speed, angular width, and position in the corona.

The 3D reconstruction indicates that the CME propagates along a radial trajectory, with a Stonyhurst latitude of −36° and longitude of 85°. The tilt angle (γ), which describes the orientation of the CME's central axis relative to the solar equatorial plane, is 90°, signifying a north–south axis. The CME speed is derived from a linear fit of the leading-front distances in GCS reconstruction, giving a value of 1700 km s^{-1}. The aspect ratio (κ) is 0.70 and the half angle is 25°. Following the approach outlined by Dumbović et al. (2019), the semi-angular width of the CME in the equatorial plane is determined using the formula: $R_{\rm maj} - (R_{\rm maj} - R_{\rm min}) \times |\gamma|/90$, where $R_{\rm maj}$ represents the face-on half-width of the CME and is obtained by adding the half-angle to $R_{\rm min}$, the edge-on half-width. The value of $R_{\rm min}$ itself is derived using arcsin(κ). This results in a width or total angular extent of the CME of 89°. Thus, the wide CME (∼89°) is propagating in IP space in the direction S36W85 with a high speed (∼1700 km s^{-1}).

5. Analysis of the SEP event on 13 May 2024

In this section, we first present the SEP event observed by near-Earth spacecraft (Wind, ACE, SOHO), STEREO-A, and JUICE on 13 May 2024, together with the IP context through which particles were accelerated and spread. We then proceed with in-depth analyses of the SEP pitch-angle distributions (PADs) and of the proton energy spectra from the three locations. Finally, we present a detailed comparison of JUICE, SOHO, and STEREO-A observations, including proton spectra analyses.

5.1. Solar energetic particle measurements and IP context

As mentioned in Sect. 4, the period of May 2024 was characterised by high levels of solar activity. In particular, a sequence of CMEs launched in close succession from AR 13664 was responsible for the largest geomagnetic storm in two decades, which took place between 10 and 12 May (e.g. Hajra et al. 2024; Liu et al. 2024; Hayakawa et al. 2025). The link to a simulation of the heliosphere's state during the aforementioned period, using the WSA–ENLIL+Cone model (Odstrcil et al. 2004), is included in Appendix A, along with a description of the model and the model's input parameters.

To evaluate the IP context through which SEPs accelerated by the 13 May eruption were spread near the locations of the Earth, JUICE, and STEREO-A, we also examined (in addition to particle data at the three locations of interest) the magnetic field and plasma measurements near Earth and at STEREO-A. We note that evaluating the IP status is crucial for understanding how particles reach the different spacecraft compared here, as IP structures can influence their fluxes and anisotropies (Richardson & Cane 1996; Rodríguez-García et al. 2025).

These combined observations of magnetic field, plasma, and particles are all displayed in Fig. 3. To identify the different structures impacting the two locations for which magnetic field and plasma data are available (i.e. Earth and STEREO-A), we searched for signatures indicating the passage of shocks as well as IP CMEs (hereafter ICMEs, e.g. Zurbuchen & Richardson 2006). The so-called magnetic clouds (displaying a clear flux rope structure) are easily identifiable via 'classic' signatures such as (1) an increase in the magnetic field strength, (2) a monotonic magnetic field rotation, (3) low proton temperature, and (4) plasma β below 1 (Burlaga et al. 1981). The event studied here features multiple instances of CME-CME interaction (e.g. Lugaz et al. 2017); hence, it is not straightforward to isolate individual eruptions in the in situ time series. Nevertheless, we attempted to separate the arrivals of distinct magnetic field and plasma environments, noting that at least a portion of them may have undergone interaction and merging before reaching 1 au. We identified a magnetic ejecta when at least the following conditions were met: plasma β below 1, a lower-than-expected temperature, some rotation in the magnetic field components, and lower fluctuations in the magnetic field in comparison to the ambient solar wind. In the following, we describe the IP context at the three locations emerging from our analysis in greater detail.

5.1.1. Solar energetic particle observations and IP context: Earth

Figure 3a shows the magnetic field, plasma, and particle observations by near-Earth spacecraft from 13 to 16 May 2024. The peak of the solar flare associated with the SEP event on 13 May is indicated with the vertical dashed purple line. At the time of the SEP onset, near-Earth spacecraft were embedded in a series of interacting magnetic ejecta indicated with the golden and aqua shadings from 07:20 UT on 13 May to 06:16 UT on 14 May. We observed rotations in the magnetic field components (iii, iv), a low plasma beta (viii), evidence of speed expansion (v), a lower-than-expected temperature (vii), and bi-directional suprathermal electron PADs. The bottom panel (x) shows the proton intensity profile as measured by ACE/EPAM, SOHO/EPHIN, and SOHO/ERNE, presenting a gradual rise of energetic protons above 13 MeV up to at least 50 MeV. We observe a flux peak around 18:00 UT on 13 May, likely related to a sudden change in the magnetic field orientation (panel (iii)). The lower ion energies only increase in the rear part of magnetic ejecta after the passage of a shock-like wave impacting near-Earth space at 23:20 UT on 13 May indicated with the grey vertical line. Protons arrived to the spacecraft from the Sun at pitch-angle 180 (inwards polarity), and present a bidirectional flow of suprathermal electrons accompanied by a depletion at a pitch angle of 90 lasting ∼12 hours, consistent with the presence of a magnetic ejecta, as discussed in Sect. 5.2. Near-Earth spacecraft also observed a prior energetic storm particle (ESP) event associated with a shock arrival on May 10 and an SEP event on May 11 followed by several ESP events associated with IP shocks arriving at Earth (not shown). This period is the one related to the intense geomagnetic storm discussed by Hajra et al. (2024), Liu et al. (2024), Hayakawa et al. (2025), and Weiler et al. (2025), for instance.

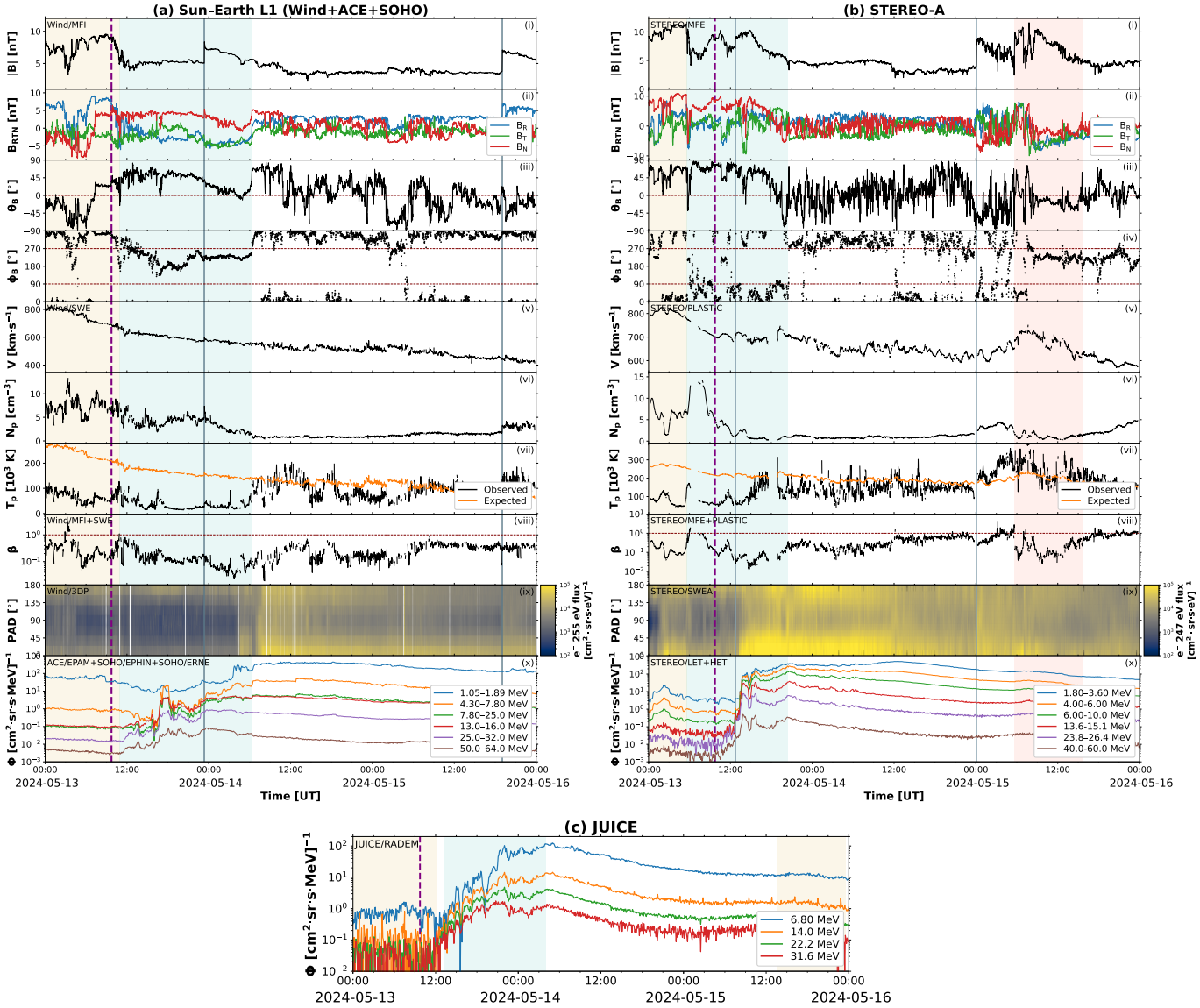

Fig. 3. In situ magnetic field and plasma observations as well as SEP time profiles by (a) near-Earth spacecraft and (b) STEREO-A, together with (c) proton observations by JUICE. The panels in (a) and (b) from top to bottom: (i) magnetic field magnitude, (ii) magnetic field components (where RTN stands for radial-tangential-normal coordinates; e.g. Hapgood 1992), magnetic field (iii) latitudinal and (iv) azimuthal angles, $\theta_{\text{B-RTN}}$ and $\phi_{\text{B-RTN}}$, (v) solar wind speed, (vi) proton density, (vii) proton temperature, (viii) plasma β, (ix) solar wind suprathermal electron PADs, and (x) energetic proton temporal profiles. The purple dashed line indicates the flare peak time (13 May 2024 at 09:44 UT). Solid gray vertical lines indicate the passage of IP shocks or shock-like structures, whilst shaded areas in alternating colours indicate magnetic ejecta. The panel in (c) shows the energetic proton temporal profiles (i) for JUICE, with the three marked magnetic ejecta regions being propagated from their corresponding passage times at STEREO-A. Further details are given in the main text.

5.1.2. Solar energetic particle observations and IP context: STEREO-A

Figure 3b shows the magnetic field, plasma, and particle observations by STEREO-A from 13 to 16 May 2024. At the time of the SEP onset, the STEREO-A spacecraft was embedded in an magnetic ejecta indicated with the aqua shading from 05:38 UT to 20:27 UT on 13 May. This is the same magnetic ejecta identified at the near-Earth location, marked with the same colour. The bottom panel (x) shows a clear proton event observed up to energies of ~40 MeV with a fast increase in the measured fluxes coinciding with the passage of a shock-like wave marked with the grey vertical line (likely corresponding to the one identified at Earth), where clear velocity dispersion is also present. We observed a double peak in the flux of protons followed by a gradual increase until the end of the magnetic ejecta, which marks the start of the decay phase of the particle enhancement. The depletion of particles in between the two peaks might be related to a sudden change in the magnetic field orientation (panel (iii)). The protons arriving first reached the spacecraft from the Sun at pitch-angle 0 (outwards polarity), as discussed in Sect. 5.2. The prior ESP event that occurred on 10 May as well as the SEP event of 11 May are also measured by STEREO-A, with proton flux profiles that are qualitatively similar to the ones detected at near-Earth spacecraft (not shown).

5.1.3. Solar energetic particle observations: JUICE

The bottom panel i of Fig. 3c shows the SEP event on 13 May 2024 observed by JUICE/RADEM, using the four resulting

channels described in Sect. 3, with effective energies of 6.9 MeV (blue line), 13.3 MeV (orange line), 21.6 MeV (green line), and 31.2 MeV (red line). The data correspond to particles coming from the anti-Sun direction, as discussed above, with a resolution of five minutes. The observed profiles show a relatively fast rise of energetic protons after the solar flare peak time that reaches energies of at least 31 MeV. The magnetometer on board JUICE was not measuring at that time; hence, it is not possible to confirm the concurrent presence of a magnetic ejecta at JUICE's location. Nevertheless, the spacecraft's proximity to STEREO-A enables us to assume that JUICE was embedded at the onset time of the 13 May SEP event in the same two interacting and merged structures indicated in Fig. 3b by the golden and aqua shaded areas.

These structures were time-shifted to JUICE, assuming average propagation speeds of 820 km s^{-1} and 710 km s^{-1}, respectively, based on PLASTIC data, which are also marked in Fig. 3c with similar colour shading. The presence of a magnetic ejecta may affect the profile of energetic protons observed by RADEM, leading to a depletion in particle flux that coincides with the centre of the structure indicated by the aqua shading, as previously observed by STEREO-A. We have also time-shifted to JUICE the small magnetic ejecta observed at STEREO-A during 15 May (salmon-shaded region), that is, towards the decay phase of the SEP event, using an average speed of 680 km s^{-1} based again on PLASTIC data.

RADEM also observed the previous SEP event on 11 May 2024 (not shown). However, this portion of the data cannot be reconstructed straightforwardly due to both the single coincidence mode of the PDH, which makes the sensors sensitive to penetrating particles above 70 MeV, and the large fluxes of high-energy particles related to the 11 May SEP event.

5.2. Solar energetic particle pitch-angle distributions

In this section, we study the PAD of STEREO-A and Wind, both of which provide energetic particle anisotropy information. Due to the different pointing directions of STEREO-A and SOHO compared to JUICE, it is necessary to analyse the PADs to identify periods of isotropy for meaningful comparison of particle fluxes. We used the 16 viewing directions of the LET instrument on board STEREO-A. It is important to note that the pitch-angle coverage provided by STEREO-A/LET is influenced by the alignment between the magnetic field and the instrument's viewing geometry. In contrast, the Wind spacecraft is spin-stabilised, with the spin axis perpendicular to the ecliptic plane and equipped with a wide-field telescope. This enables the 3DP instrument to sample a broader portion of the sky, allowing for a more comprehensive reconstruction of the three-dimensional particle distribution.

5.2.1. Solar energetic particle pitch-angle distributions: Earth

Figure 4(a) shows the PAD of protons measured by Wind/3DP at 4 MeV. Panel (i) shows the intensities observed by each pitch-angle bin, while panel (ii) shows the pitch-angle coverage of each of the eight publicly available pitch-angle bins of the instrument. Panel (iii) presents the PAD with colour-coded intensities and panel (iv) indicates the first-order anisotropy, in the range of [−3, 3] (e.g. Dresing et al. 2014) and the second-order anisotropy. We note that periods are considered isotropic when the first and second-order anisotropy is low, $\lesssim|1|$. This panel shows that the early phase of the ∼3.1–5.7 MeV proton event is anisotropic for more than twelve hours, showing also a strong bidirectional component. From the onset of the SEP event, shortly after the soft-X ray peak of the flare indicated with the vertical line, and until 06:00 UT on 14 May, we observe higher fluxes in the bins measuring particles coming from the Sun (panel (i)). These correspond to pitch angles near 180° (panel (ii)), consistent with the local negative magnetic polarity shown in Fig. 3a. Starting around midday on 13 May and lasting for approximately twelve hours, we observe a bidirectional flow along the magnetic field (pitch angles of 0° and 180°) with a depletion in intensity around pitch angles of 90°. This feature is characterised by the large second-order anisotropy (panel iii) and is consistent with the presence of a magnetic ejecta, as discussed in Sect. 5.1.1. After this period, the first-order anisotropy becomes positive, consistent with the sunward-looking bins observing higher fluxes of particles with pitch angles near 0°. During the decay phase of the SEP event, from 15 to 16 May the flux becomes isotropic; namely, the first-order anisotropy is ∼0. We indicate in Fig. 4a the period selected for the intercalibration analysis with the grey shading. This is further discussed below.

5.2.2. Solar energetic particle pitch-angle distributions: STEREO-A

Panel b of Fig. 4 displays proton intensities in the 6–10 MeV range as measured by STEREO-A/LET across its 16 sectors, with eight forward-facing sectors represented in shades of red and eight rear-facing sectors shown in shades of blue. LET measured an 18-hour anisotropic period starting shortly after 12:00 UT on 13 May, where most of the particles are observed in the sunward-facing sectors. The vertical line indicates the soft-x ray flare peak time. The pitch-angle coverage is not good during the SEP onset period, only covering 60−120° as shown in panel (ii), which presents the pitch-angles of the sector centres. During the decay phase of the SEP event, from 15 to 17 May, the flux becomes isotropic. We selected the period 12:00 UT to 18:00 UT on 15 May, as the time with the lowest first-order anisotropy value, marked by the grey shading in the figure, for use in the intercalibration analysis, as discussed in Sect. 5.4. We note that, in selecting the grey-shaded area, we intentionally excluded the period from 18:00 UT on 15 May to 02:00 UT on 16 May. This was because, even though the anisotropy remains very low, the pitch-angle coverage changes, as shown in panel (ii).

5.3. Comparison between JUICE, STEREO-A, and near-Earth measurements

Figure 5 shows the time profiles for each of the four effective energies, namely 6.9, 13.3, 21.6, and 31.2 MeV measured by JUICE (magenta) and the correspondent channels at STEREO-A (red) and near-Earth (green), as shown in the legend. STEREO-A presents the most prompt increase in the signal of protons reaching the peak intensity shortly after the SEP event onset. We note that the presence of the magnetic ejecta, indicated by the aqua-shaded area marking its arrival at STEREO-A, modulated the particle profile, causing rapid decreases and increases in their fluxes, as discussed in Sect. 5.1.2. The JUICE spacecraft also measures similar peak proton fluxes but with a slower increase, probably related to the anti-Sun–spacecraft-line pointing of the instrument. Wind and SOHO show a slower increase and lower peak intensities that might be related to their worse magnetic connectivity as discussed in Sect. 2.

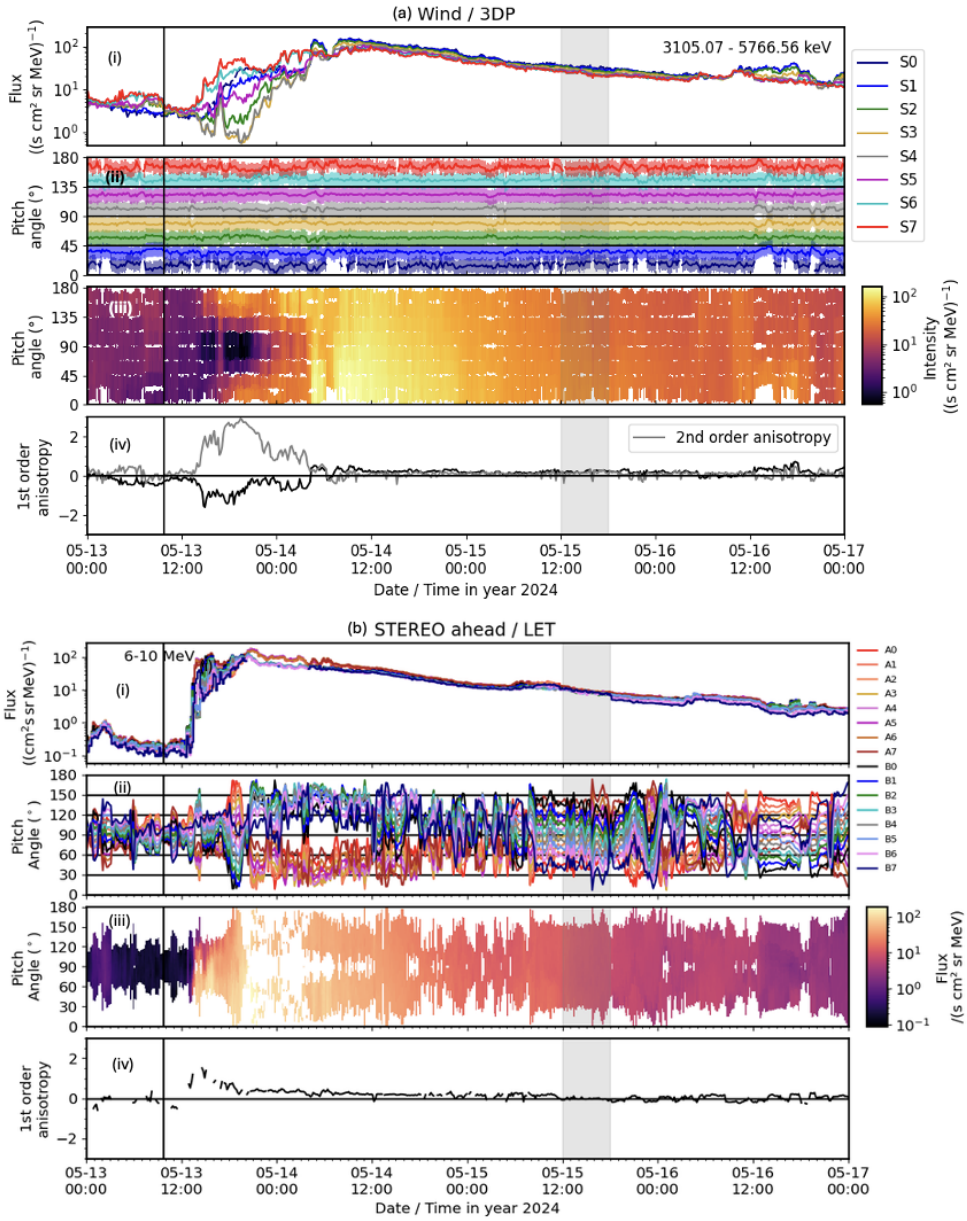

Fig. 4. Pitch-angle distributions of protons recorded by Wind/3DP at 4 MeV (panel a) and STEREO-A/LET at 6 MeV (panel b). The panels include: (i) the measured intensities within each instrument's field of view; (ii) the pitch-angle coverage, displayed for the eight angular bins of Wind/3DP (a) and the central angles of 16 STEREO-A/LET sectors (b), with front-facing sectors shown in red hues and rear-facing in blue hues; (iii) a colour-coded representation of the pitch-angle intensity distribution; and (iv) first-order anisotropy values, ranging from −3 to 3, following the approach of Dresing et al. (2014). A vertical line marks the timing of the soft X-ray flare peak (approximately 09:44 UT), which is linked to the associated SEP event. Details given in the main text.

The main difference in the flux of particles between STEREO-A/LET and HET, and JUICE/RADEM, as measured by the four proton channels of Fig. 5, occurs during the SEP onset, namely between the flare peak time indicated with the dashed vertical line and middle of day 14 May 2024. This disparity might be partly related to the difference in the field of view, as the period mentioned above is anisotropic as discussed in Sect. 5.2. We note again that JUICE/RADEM is looking away from the Sun in the radial direction, while STEREO-A/LET fluxes are summed along the 16 sectors and STEREO-A/HET HET is viewing along the nominal Parker spiral.

We also show in the first panel of Fig. 5 the fluxes measured by STEREO-A/LET (gray line) only in sector B7, namely looking against the direction of the Sun, with a field of view of 25°, similar to the JUICE/RADEM field of view. We note that this STEREO-A/LET sectored data set is only available for the ∼7.7 MeV proton energy channel. In Appendix B we explain the reason behind the data gap shown in the B7 sectored data. We observed a dissimilarity in the fluxes measured by JUICE (magenta line) in comparison to STEREO-A/LET/B7 (grey line). Although this could be related to not being exactly observing the same field of view, the fact that the internal structures of the magnetic ejecta pass by STEREO-A and JUICE at different times (potentially modulating the particle profile differently) could be an important factor.

With a lower impact, the difference in radial distance between STEREO-A and JUICE (0.13 au) might be also affecting the measured fluxes of particles. As demonstrated, for

example, by Lario et al. (2006) and Rodríguez-García et al. (2023), SEP intensities tend to depend on heliocentric distance. To evaluate this effect on the difference in the flux measured by JUICE, we applied a radial scaling in the fluxes. Figure 5 shows the JUICE intensity values, corrected (I_{corr}) for radial distance, as indicated by the purple-shaded curve. We scaled it to the location of STEREO-A, with corrected peak intensities calculated as a radial dependence of $R^{\alpha_{rad}}$ as detailed by Lario et al. (2006), namely $\alpha_{rad} = \log(I_{observed}/I_{corrected})/\log(R_{observed}/R_{corrected})$, where $\alpha_{rad} = a \pm b$, and $a = 2.14$, $b = 0.26$ for 4–13 MeV protons, and $a = 1.97$, $b = 0.27$ for 27–37 MeV protons, which are based on the radial distributions obtained by Lario et al. (2006). As illustrated in the figure, the radial correction is small compared to the differences between the STEREO-A and JUICE intensities.

In Fig. 5, we use the grey hatched area to show the isotropic period described in Sect. 5.2. This period partially coincides with a magnetic ejecta structure arriving at STEREO-A, indicated with the salmon shading, which apparently did not influence the isotropisation of the proton fluxes. The three locations (near-Earth assets, STEREO-A, and JUICE) exhibit very similar proton temporal profiles, as the particles may be uniformly distributed in longitude and radial distance within the heliosphere due to the reservoir effect, with comparable intensities observed between the distant spacecraft (McKibben 1972; Roelof et al. 1992; Lario 2010).

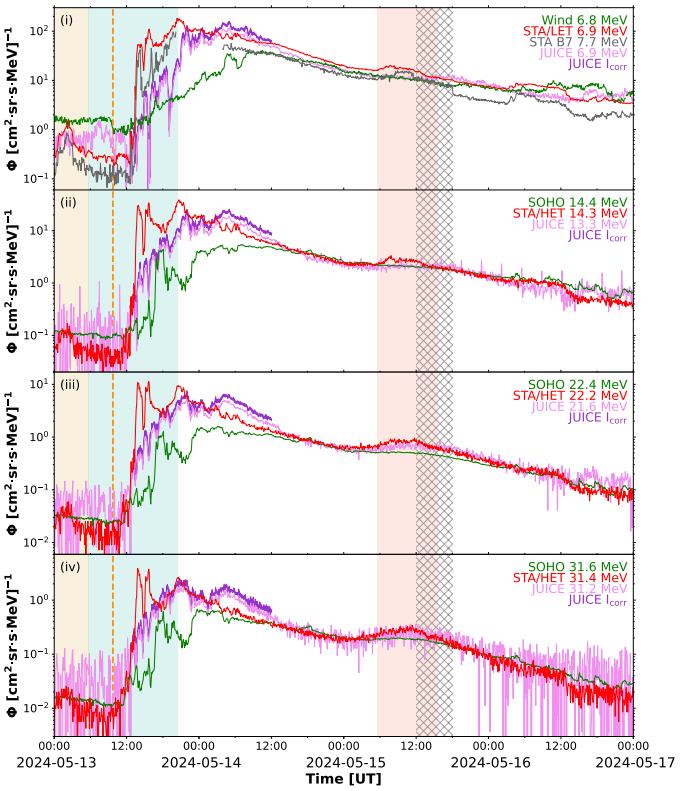

Fig. 5. In situ SEP time profiles by Wind/3DP (omni) or SOHO/ERNE (sun) in green, STEREO-A/LET (omni) or HET (sun) in red, and JUICE/RADEM (anti-sun) in magenta for four different proton energies: (i) ~6.9 MeV, (ii) ~13.3, (iii) ~21.6 MeV, and (iv) ~31.2 MeV. The value of JUICE I_{corr} was estimated applying a radial scaling in the fluxes to STEREO-A location. The orange dashed line in the four panels indicates the flare peak time, while the various shadings mark the magnetic ejecta present at the location of STEREO-A, discussed in Sect. 5.1.2, and the gray hatched area the isotropic period, discussed in Sect. 5.2. Further details are given in the main text.

5.4. Energy proton spectra and intercalibration analysis

To perform a cross-calibration of the energetic particle instruments on board the JUICE and STEREO-A spacecraft, we determined the proton spectra, as observed by STEREO-A during the isotropic period. This interval spans from 12:00 UT to 18:00 UT on 15 May 2024, as indicated by the grey shading in Figs. 4 and 5 (hatched). We used the omnidirectional data from STEREO-A/LET and HET (Sun-directed) and following the method described by Dresing et al. (2020) and Strauss et al. (2020) we fit the spectrum using orthogonal distance regression (ODR; Boggs & Rogers 1989) provided by the SciPy Python package (Virtanen et al. 2020). We note that in contrast to the approach of Dresing et al. (2020) and Strauss et al. (2020), here we used the errors of the fit parameters as returned by ODR, which represent the standard deviations of the estimated parameters. We found a broken power law to best describe the data represented by

$$I(E) = I_0 \left(\frac{E}{E_0}\right)^{\delta_1} \left(\frac{E^\alpha + E_b^\alpha}{E_0^\alpha + E_b^\alpha}\right)^{\frac{\delta_2 - \delta_1}{\alpha}} . \quad (1)$$

This model yields a spectral transition at the energy E_b, where δ_1 and δ_2 are the spectral indices at energies below and above E_b. The parameter α describes the sharpness of the spectral transition and E_0 is a reference energy at 0.1 MeV. The results are shown in Fig. 6, where STEREO-A/LET and HET are shown with the reddish points. The spectral index below (above) the spectral transition is $\delta_1 = -2.26 \pm 0.05$ ($\delta_2 = -6.46 \pm 1.92$), where the spectral break and transition energy is $E_b = 33.9 \pm 8.2$ MeV. We note the high uncertainty in the second spectral index. Modifying the time period chosen for the accumulated spectrum (not shown) alters the spectral transition energy, potentially influencing the intercalibration factor for the fourth JUICE energy channel.

We also show in Fig. 6 the accumulated spectrum as measured by SOHO/ERNE (black points). We note that five out of seven points almost perfectly agree with the fit based on STEREO-A data. For the determination of an intercalibration factor for JUICE/RADEM, we used the spectral fit from STEREO-A as the reference for the particle environment measured by JUICE and estimated the ratios in the proton flux measured by JUICE (magenta points) compared to the fit. We did not apply any radial or longitudinal scaling for the spacecraft measurements based on the reservoir effect discussed in Sect. 5.3. Table 2 shows the derived intercalibration factors of each of the effective energy channels of JUICE/RADEM. The proton fluxes measured at the effective energies of 6.9, 13.3, 21.6, and 31.2 MeV by the radiation monitor onboard JUICE agree with the STEREO-A measurements, with a deviation of less than 25%. We note that the smallest intercalibration factors, specifically 1.02 and 0.95, were obtained for the first (6.9 MeV) and last (31.2 MeV) channel, respectively, for which the quality of the data reconstruction is better (as described in Sect. 3).

6. Summary and discussion

JUICE was launched in April 2023, and it is now in its cruise phase to Jupiter, where it is scheduled to arrive in July 2031. JUICE carries RADEM, a radiation monitor that operates continuously to measure protons, electrons, and ions, pointing mainly

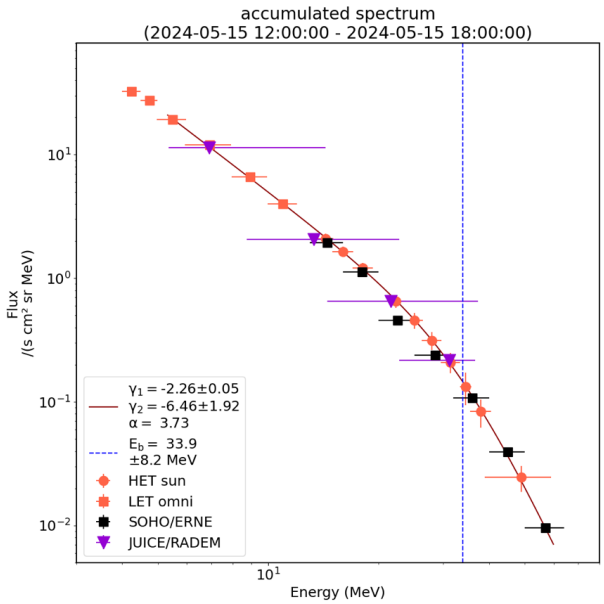

Fig. 6. Proton-accumulated spectra measured by STEREO-A (red), SOHO/ERNE (black), and JUICE/RADEM (magenta). The legend shows the fit values using STEREO-A data: the spectral index (δ_1, δ_2) observed in between the spectral transition: E_b; and α, which determines the sharpness of the break (Strauss et al. 2020). Details are given in the main text.

in the anti-Sun–spacecraft direction. One of its instruments, the PDH is an eight-sensor silicon stack detector with a field of view of 20°, configured from September 2023 to July 2024 in a single-coincidence mode (i.e. each sensor was working independently). After linearly combining the bins and applying a bow-tie method (described in Sect. 3), we derived four differential channels with effective energies of 6.9, 13.3, 21.6, and 31.2 MeV. These are summarised in Table 1.

Over the month of May 2024, AR 13664 produced a series of CMEs and associated SEP events. This period is the one related to the intense geomagnetic storm discussed a number of authors, including Hajra et al. (2024), Liu et al. (2024), Hayakawa et al. (2025), and Weiler et al. (2025). On 13 May 2024, a large SEP event took place in association with an eruption close to the western limb of the Sun as seen from Earth (Fig. 2). Several spacecraft in the heliosphere observed the SEP event, including JUICE, STEREO-A, near-Earth spacecraft (Wind, ACE, SOHO), PSP, and Solar Orbiter, as shown in the proton flux profiles in Fig. 1b. Providentially, at that time JUICE was located very close to STEREO-A, with a difference of 0.13 au in radial distance, 0.3° in latitude, and 1.6° in longitude, as shown in Fig. 1a. Therefore, in this study, we have aimed to characterise JUICE observations and perform a cross-calibration of the energetic particle instruments aboard the JUICE and STEREO-A spacecraft.

For this purpose, we focussed our analysis on spacecraft located near 1 au, namely JUICE, STEREO-A, and near-Earth assets, all of which were well connected to the parent solar source. This is shown in Fig. 1a, using the nominal Parker spirals. To evaluate the IP context through which SEPs accelerated by the 13 May eruption were spread, we examined the particle data from the three locations of interest, along with the magnetic field and plasma measurements near Earth and at STEREO-A (Fig. 3). At the time of the SEP event, STEREO-A was embedded in a magnetic ejecta, which was likely also present at JUICE's location, since the magnetometer on JUICE was not operating to confirm this.

Table 2. Intercalibration factors between STEREO-A and JUICE.

JUICE Eff (range, MeV)	Intensity ratio (STA/JUICE)
6.9 (5.35–14.35)	1.02
13.3 (8.75–22.75)	1.23
21.6 (14.50–37.37)	1.12
31.2 (22.80–36.60)	0.95

We studied the proton anisotropies measured by Wind and STEREO-A. We found anisotropic periods lasting a few hours during the SEP onset, which evolved into an isotropic period during the decay phase of the event, as shown in Fig. 4. We selected the period from 12:00 UT to 18:00 UT 15 May as the interval with the lowest first-order anisotropy at the location of STEREO-A, indicated by the gray shading in Fig. 4.

In Fig. 5, we compare the proton flux observations of the three selected spacecraft for similar energies to the four effective channels of JUICE. We observed dissimilarities at the onset of the SEP event due to several factors: the different fields of view of the spacecraft, the local magnetic ejecta, and, to a lesser extent, the varying radial distances. However, during the period indicated by the grey hatched area in Fig. 5, corresponding to the selected isotropic period, the three spacecraft exhibit similar proton fluxes.

We therefore considered the isotropic period during the decay phase of the SEP event to compute the accumulated proton spectrum for the three spacecraft. We note that the selection of this isotropic period for comparison with JUICE is particularly important, as RADEM primarily observes particles coming from the anti-Sun direction. We fit the STEREO-A spectra with a double power law, as shown in Fig. 6. The results of the fit showed no significant variation within the sub-periods of the selected period (not shown), except for the second spectral index, which exhibited larger uncertainty. The different channels of the near-Earth proton spectra agreed closely with the STEREO-A fit.

We considered STEREO-A spectral fit as the particle environment measured by JUICE and estimated the differences in the proton flux measured by JUICE in comparison with the fit. Based on the results shown in Fig. 6 and summarised in Table 2, the proton fluxes measured at the effective energies of 6.9, 13.3, 21.6, and 31.2 MeV by the radiation monitor onboard JUICE are in agreement (with a deviation of less than 25%) with respect to STEREO-A measurements.

We note that the results obtained in this study are valid only for RADEM data collected before 10 July 2024, when the instrument's configuration was changed. We also note that the method used here for the intensity comparison carries some uncertainties. While this method finds a unique value of $G \cdot dE$ to reconstruct the RADEM flux independently of the spectral index, the response of each channel still depends on it. Therefore, the quality of the RADEM intensity reconstruction is influenced by the spectral shape at each moment in time. In a future work, we will examine other SEP events with different particle spectral shapes to compare the intercalibration results.

7. Conclusions

This work illustrates that the RADEM instrument on board JUICE is a valuable tool for measuring SEP events in the heliosphere, providing an excellent opportunity to study and characterise the energetic particle environment in the solar wind between 0.65 and 5.2 au. The proton fluxes measured at the effective energies of 6.9, 13.3, 21.6, and 31.2 MeV by RADEM are in agreement, with a deviation less than 25%, with STEREO-A measurements. The intercalibration factors between STEREO-A and JUICE are 1.02, 1.23, 1.12, and 0.95, respectively. We note that this result is valid only for RADEM data collected before 10 July 2024.

Acknowledgements. L.R.-G. acknowledges support through the European Space Agency (ESA) research fellowship programme. L.R.-G. and E.P. acknowledge support from ESA through the Science Faculty – Funding reference ESA-SCI-E-LE-050. E.P. also acknowledges support from NASA's HGIO (no. 80NSSC23K0447), LWS (no. 80NSSC19K0067), and LWS-SC (no. 80NSSC22K0893) programmes. N.D. and J.G. acknowledge funding from the European Union's Horizon Europe research and innovation programme under grant agreement No. 101134999 (SOLER). The paper reflects only the authors' view and the European Commission is not responsible for any use that may be made of the information it contains. Work in the University of Turku was performed under the umbrella of Finnish Centre of Excellence in Research of Sustainable Space (FORESAIL) funded by the Research Council of Finland (grant No. 352847). N.D. is grateful for support by the Research Council of Finland (SHOCKSEE, grant No. 346902). We also thank the members of the Data Analysis Working Group at the Space Research Laboratory of the University of Turku, Finland for useful discussions. The UAH team acknowledges the financial support of MICIU/AEI/10.13039/501100011033 and FEDER, UE through project PID2023-150952OB-I00. C.M.S.C. acknowledges additional partial funding from NASA grants 80NSSC22K0893, 80NSSC21K1327, 80NSSC20K1815, and 80NSSC19K0067. The authors thank NASA's Community Coordinated Modeling Center (CCMC; https://ccmc.gsfc.nasa.gov) for supporting the WSA–ENLIL+Cone simulation efforts presented in this work. The WSA model was developed by C. N. Arge (currently at NASA Goddard Space Flight Center) and the ENLIL model was developed by D. Odstrcil (currently at George Mason University). The WSA–ENLIL+Cone simulation run employed in this work can be accessed online at https://ccmc.gsfc.nasa.gov/ungrouped/SH/Helio_main.php (run id: *Laura_Rodriguez-Garcia_092424_SH_1*).

References

Acuña, M. H., Curtis, D., Scheifele, J. L., et al. 2008, Space Sci. Rev., 136, 203
Allison, J., Amako, K., Apostolakis, J., et al. 2016, Nuclear Instruments and Methods in Physics Research Section A: Accelerators, Spectrometers Detectors and Associated Equipment, 835, 186
Benkhoff, J., Murakami, G., Baumjohann, W., et al. 2021, Space Sci. Rev., 217, 90
Boggs, P. T., Rogers, J. E. 1989, Contemp. Math., Vol. 112, Statistical Analysisof Measurement Error Models and Applications (Arcata, CA, 1989) (Amer. Math. Soc., Providence, RI), 183
Burlaga, L., Sittler, E., Mariani, F., & Schwenn, R. 1981, J. Geophys. Res., 86, 6673
Case, A. W., Kasper, J. C., Stevens, M. L., et al. 2020, ApJS, 246, 43
Domingo, V., Fleck, B., & Poland, A. I. 1995, Sol. Phys., 162, 1
Dresing, N., Gómez-Herrero, R., Heber, B., et al. 2014, A&A, 567, A27
Dresing, N., Effenberger, F., Gómez-Herrero, R., et al. 2020, ApJ, 889, 143
Dresing, N., Rodríguez-García, L., Jebaraj, I. C., et al. 2023, A&A, 674, A105
Dresing, N., Jebaraj, I. C., Wijsen, N., et al. 2025, A&A, 695, A127
Dumbović, M., Guo, J., Temmer, M., et al. 2019, ApJ, 880, 18
Fox, N. J., Velli, M. C., Bale, S. D., et al. 2016, Space Sci. Rev., 204, 7
Galvin, A. B., Kistler, L. M., Popecki, M. A., et al. 2008, Space Sci. Rev., 136, 437
Gieseler, J., Dresing, N., Palmroos, C., et al. 2023, Front. Astron. Space Sci., 9, 384
Gold, R. E., Krimigis, S. M., Hawkins, S. E., I., , et al. 1998, Space Sci. Rev., 86, 541
Grasset, O., Dougherty, M. K., Coustenis, A., et al. 2013, Planet. Space Sci., 78, 1
Hajdas, W., Gonçalves, P., Pinto, M., et al. 2025, Space Science Reviews, 221, 43
Hajra, R., Tsurutani, B. T., Lakhina, G. S., Lu, Q., & Du, A. 2024, ApJ, 974, 264
Hapgood, M. A. 1992, Planet. Space Sci., 40, 711
Hayakawa, H., Ebihara, Y., Mishev, A., et al. 2025, ApJ, 979, 49
Howard, R. A., Moses, J. D., Vourlidas, A., et al. 2008, Space Sci. Rev., 136, 67
Jiggens, P., Chavy-Macdonald, M.-A., Santin, G., et al. 2014, J. Space Weather and Clim., 4, A20
Kaiser, M. L., Kucera, T. A., Davila, J. M., et al. 2008, Space Sci. Rev., 136, 5
Kasper, J. C., Abiad, R., Austin, G., et al. 2016, Space Sci. Rev., 204, 131
Khoo, L. Y., Sánchez-Cano, B., Lee, C. O., et al. 2024, ApJ, 963, 107
Kollhoff, A., Kouloumvakos, A., Lario, D., et al. 2021, A&A, 656, A20
Kruparova, O., Krupar, V., Szabo, A., et al. 2024, ApJ, 970, L13
Lario, D. 2010, in Twelfth International Solar Wind Conference, eds. M. Maksimovic, K. Issautier, N. Meyer-Vernet, M. Moncuquet, & F. Pantellini, AIP Conf. Ser., 1216, 625
Lario, D., Kallenrode, M.-B., Decker, R. B., et al. 2006, ApJ, 653, 1531
Lario, D., Wijsen, N., Kwon, R. Y., et al. 2022, ApJ, 934, 55
Lemen, J. R., Title, A. M., Akin, D. J., et al. 2012, Sol. Phys., 275, 17
Lepping, R. P., Acũna, M. H., Burlaga, L. F., et al. 1995, Space Sci. Rev., 71, 207
Lin, R. P., Anderson, K. A., Ashford, S., et al. 1995, Space Sci. Rev., 71, 125
Liu, Y. D., Hu, H., Zhao, X., Chen, C., & Wang, R. 2024, ApJ, 974, L8
Lugaz, N., Temmer, M., Wang, Y., & Farrugia, C. J. 2017, Sol. Phys., 292, 64
Luhmann, J. G., Curtis, D. W., Schroeder, P., et al. 2008, Space Sci. Rev., 136, 117
McComas, D. J., Alexander, N., Angold, N., et al. 2016, Space Sci. Rev., 204, 187
McKibben, R. B. 1972, J. Geophys. Res., 77, 3957
Mewaldt, R. A., Cohen, C. M. S., Cook, W. R., et al. 2008, Space Sci. Rev., 136, 285
Müller, D., St. Cyr, O. C., Zouganelis, I., et al. 2020, A&A, 642, A1
Müller-Mellin, R., Kunow, H., Fleißner, V., et al. 1995, Sol. Phys., 162, 483
Odstrcil, D., Riley, P., & Zhao, X. P. 2004, Journal of Geophysical Research (Space Physics), 109, A02116
Ogilvie, K. W., & Desch, M. D. 1997, Adv. S, 20, 559
Ogilvie, K. W., Chornay, D. J., Fritzenreiter, R. J., et al. 1995, Space Sci. Rev., 71, 55
Owen, C. J., Bruno, R., Livi, S., et al. 2020, A&A, 642, A16
Palmerio, E., Kilpua, E. K. J., Witasse, O., et al. 2021, Space Weather, 19, e2020SW002654
Pesnell, W. D., Thompson, B. J., & Chamberlin, P. C. 2012, Sol. Phys., 275, 3
Pinto, M. 2019, PhD thesis, University of Lisbon - Instituto Superior Tecnico
Pinto, M., Goncalves, P., Hajdas, W., & Socha, P. 2020, European Planetary Science Congress, EPSC2020-311
Raukunen, O., Paassilta, M., Vainio, R., et al. 2020, Journal of Space Weather and Space Climate, 10, 24
Richardson, I. G., & Cane, H. V. 1996, J. Geophys. Res., 101, 27521
Rodríguez-García, L., Gómez-Herrero, R., Zouganelis, I., et al. 2021, A&A, 653, A137
Rodríguez-García, L., Gómez-Herrero, R., Dresing, N., et al. 2023, A&A, 670, A51
Rodríguez-García, L., Gómez-Herrero, R., Dresing, N., et al. 2025, A&A, 694, A64
Rodríguez-Pacheco, J., Wimmer-Schweingruber, R. F., Mason, G. M., et al. 2020, A&A, 642, A7
Roelof, E. C., Gold, R. E., Simnett, G. M., et al. 1992, Geophys. Res. Lett., 19, 1243
Sánchez-Cano, B., Witasse, O., Knutsen, E. W., et al. 2023, Space Weather, 21, e2023SW003540
Sauvaud, J. A., Larson, D., Aoustin, C., et al. 2008, Space Sci. Rev., 136, 227
Stone, E. C., Frandsen, A. M., Mewaldt, R. A., et al. 1998, Space Sci. Rev., 86, 1
Strauss, R. D., Dresing, N., Kollhoff, A., & Brüdern, M. 2020, ApJ, 897, 24
Thernisien, A. F. R., Howard, R. A., & Vourlidas, A. 2006, ApJ, 652, 763
Thernisien, A., Vourlidas, A., & Howard, R. A. 2009, Sol. Phys., 256, 111
Torsti, J., Valtonen, E., Lumme, M., et al. 1995, Sol. Phys., 162, 505
Van Allen, J. A., Baker, D. N., Randall, B. A., & Sentman, D. D. 1974, J. Geophys. Res., 79, 3559
Virtanen, P., Gommers, R., Oliphant, T. E., et al. 2020, Nature Methods, 17, 261
von Rosenvinge, T. T., Reames, D. V., Baker, R., et al. 2008, Space Sci. Rev., 136, 391
Weiler, E., Möstl, C., Davies, E. E., et al. 2025, Space Weather, 23, e2024SW004260
Whitman, K., Egeland, R., Richardson, I. G., et al. 2023, Adv. Space Res., 72, 5161
Wiedenbeck, M. E., Angold, N. G., Birdwell, B., et al. 2017, International Cosmic Ray Conference, 301, 16
Zurbuchen, T. H., & Richardson, I. G. 2006, Space Sci. Rev., 123, 31

Appendix A: ENLIL simulation

ENLIL is a three-dimensional, time-dependent magnetohydrodynamic (MHD) model designed to simulate the heliospheric environment beyond 21.5 solar radii. A detailed description of the model can be found in Appendix A by Rodríguez-García et al. (2025). The state of the heliosphere and interactions with interplanetary structures present at the time of the SEP event can significantly affect spacecraft magnetic connectivity. To account for these influences, the ENLIL simulation was run from 8 to 18 May, covering five days before and after the event. This period includes earlier CMEs that could affect particle propagation and tracks the evolution of ICMEs through the interplanetary medium out to 2.1 au. The 3D parameters for seven relevant CMEs occurring between 8 and 13 May were taken from Liu et al. (2024) for use in the simulation. The parameters for the CME and model setup, along with the simulation results, can be accessed on the Community Coordinated Modeling Center (CCMC) website.[1].

Appendix B: STEREO-A threshold mode

The 13 May 2024 SEP event was large enough that STEREO-A/LET went into dynamic threshold mode. It means that the B7 sectored data for protons and He (as that is one of the detectors affected) was not available during mode 2 (Mewaldt et al. 2008). Mode 2 was on from 13 May 2024 at 20:14 UT to 14 May at 03:58 UT, as shown in the data gap in panel (i), grey line, in Fig. 5. To estimate the flux measured by STEREO-A/LET/B7 sectored data during the gap, we followed the approximation method explain below. We used the CNO energy sectored rates that were available and took a ratio between the averaged sectors B3 and B4 to sector B7, as CNO should not be affected by the dynamic thresholds. Then, we used this ratio to scale the H averaged sectors B3 and B4 data to get an approximation of what sector B7 should be measuring during this time. We note that we assumed that CNO has the same anisotropy that H has and that the composition did not change during this time period. Figure B.1 presents the result of this assumption, showing that the CNO proxy follows the trend of the gray line representing the B7 sector.

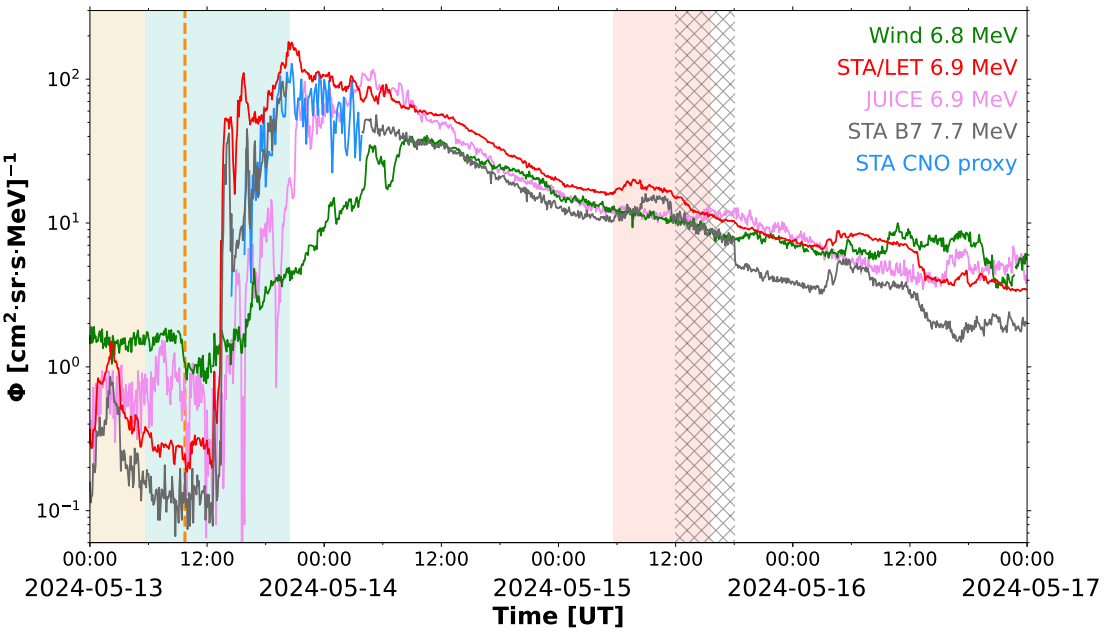

Fig. B.1. In situ proton time profiles by Wind/3DP (omni) in green, STEREO-A/LET (omni) in red, STEREO-A/LET–B7 sector in grey, STEREO-A/LET CNO proxy in blue blue, and JUICE/RADEM (anti-Sun) in magenta for ~6.9 MeV. Shading and lines are shown as in Fig. 5.

[1] https://ccmc.gsfc.nasa.gov/results/viewrun.php?domain=SH&runnumber=Laura_Rodriguez-Garcia_092424_SH_1